Research Article

Nano Research
2023, 16(7): 10234–10244

ISSN 1998-0124 CN 11-5974/O4
https://doi.org/10.1007/s12274-023-5642-x

ChemFET gas nanosensor arrays with alignment windows for assembly of single nanowires

Ondřej Chmela[1,2] (✉), Imrich Gablech[1,2], Jakub Sadílek[1,2], Jan Brodský[1], and Stella Vallejos[1,2,3] (✉)

[1] *Central European Institute of Technology, Brno University of Technology, Purkyňova 123, 61200 Brno, Czech Republic*
[2] *Faculty of Electrical Engineering and Communication, Brno University of Technology, Department of Microelectronics, Technická 3058/10, 61200 Brno, Czech Republic*
[3] *Instituto de Microelectrónica de Barcelona (IMB-CNM, CSIC), Campus UAB, Carrer dels Til·lers, Cerdanyola del Vallès, 08193 Barcelona, Spain*

Received: 13 January 2023 / **Revised:** 24 February 2023 / **Accepted:** 5 March 2023

ABSTRACT

This work focuses on the fabrication and characterization of Chemical Field-Effect Transistor (ChemFET) gas nanosensor arrays based on single nanowire (SNW). The fabrication processes include micro and nanofabrication techniques enabled by a combination of ultraviolet (UV) and e-beam lithography to build the ChemFET structure. Results show the integration and connection of SNWs across the multiple pairs of nanoelectrodes in the ChemFET by dielectrophoresis process (DEP) thanks to the incorporation of alignment windows (200–300 nm) adapted to the diameter of the NWs. Measurements of the SNW ChemFET array's output and transfer characteristics prove the influence of gate bias on the drain current regulation. Tests upon hydrogen (H_2) and nitrogen dioxide (NO_2) as analyte models of reducing and oxidizing gases show the ChemFET sensing functionality. Moreover, results demonstrate better response characteristics to H_2 when the ChemFET operates in the subthreshold regime. The design concepts and methods proposed for fabricating the SNW-based ChemFET arrays are versatile, reproducible, and most likely adaptable to other systems where SNW arrays are required.

KEYWORDS

Chemical Field-Effect Transistor (ChemFET) nanosensors, nanowires, nanoelectrodes, gas sensors

1 Introduction

In the past years, gas-sensitive nanowires, nanobelts, and nanorods, belonging to the group of one-dimensional (1D) semiconducting metal-oxide (MOX) nanostructures, have attracted considerable attention in the field of chemical (gas) sensors due to their capability to improve sensor's functionality by enhancing the surface response as opposed to alternative structures with boundary connection effect [1–3]. These structures also adapt better to the sensor's miniaturization, providing further advantages of size and cost production compared to other chemical sensors (e.g., operating with electrochemical principles [4, 5].

Usually, the gas sensors based on 1D MOX nanostructures are assembled as chemoresistive (two-electrode) or Chemical Field-Effect Transistor (ChemFET) (three-electrode) devices. In chemoresistive and ChemFET sensors, the electrical transport through the 1D MOX nanostructure(s) is modulated by the gas-solid interactions at the MOX surface. However, in ChemFET, the conductive channel can also be modulated by applying a voltage potential to the third electrode, regularly integrated as a bottom (back) gate electrode, bringing the possibility of tunning further the gas sensor response and dynamics [6–9]. Hence, the fabrication of ChemFET structures requires more elements with respect to a chemoresistor adding complexity to the fabrication process of these sensor devices.

Our previous studies on nanowire-based gas sensors have generally focused on chemoresistive structures with multiple or single nanowires, demonstrating the advantage of such systems over traditional nanoparticle-based sensors [10, 11]. Further works in the literature have also shown that a single or few nanowire structures connected in parallel are the ideal architectures to detect the external stimuli coming from the adsorption of gaseous molecules at the nanowire surface more efficiently [1, 12–15]. However, current methods for assembling aligned and isolated single nanowire (SNW) structures in chemoresistive or ChemFET configuration still represent a technological challenge. Sometimes, this challenge is overcome by connecting a unique 1D nanostructure (chosen from various random 1D nanostructures dispersed over a substrate) via focus ion beam (FIB), although this method restricts the scalability of the process and increases the cost and time of fabrication [16, 17].

Alternative routes for the alignment of 1D nanostructures (amongst them, the Langmuir-Blodgett and the electric/magnetic fields assisted techniques) have been shown to be appropriate for aligning various 1D nanostructures [18]. However, face to the on-chip integration, techniques assisted by electric field via dielectrophoresis process (DEP) may represent a technological advantage. The DEP allows aligning and connecting NWs suspended in a droplet solution by applying a nonuniform electric field that creates a dipole moment on the NWs, causing the droplet to be electrostatically pulled toward the biased electrodes. As such, this process may facilitate precise placement and lining up of several 1D nanostructures in parallel [19, 20]. However, the

Address correspondence to Ondřej Chmela, ondrej.chmela@ceitec.vutbr.cz; Stella Vallejos, stella.vallejos@imb-cnm.csic.es

integration of isolated single 1D nanostructures may depend further on the characteristics of the electrodes and the electrical environment.

Our previous studies on chemoresistive nanosensors, for instance, demonstrated that the use of several pairs of electrodes with nanoscale features facilitates to some extent the integration of isolated SNWs [10]. Recently, we have also noticed that the incorporation of dielectric shielding windows further favors the electrical environment for the integration of isolated SNWs, avoiding the aggregation of multiple NWs within a pair of nanoelectrodes. In this context, herein, we further improve the SNW arrays reported earlier [10] by developing new structures that operate with the ChemFET principles to tune the sensor response thanks to the buried gate electrode and locally drain-source (faced) electrodes nano-shaped by electron beam lithography (EBL) technique. As a novelty, the present work also explores the incorporation of alignment windows over the top of the ChemFET structure to confine the SNWs integrated across the drain-source nanoelectrodes. The gas sensing functionality of these structures is validated in the ChemFET regime using nitrogen dioxide and hydrogen gases as oxidizing and reducing model analytes.

2 Experimental

2.1 Design and layout of ChemFET nanosensors platform

We designed a layout containing several chips on a 4-inch wafer. Each chip has a size of 5 mm × 5 mm and incorporates four independent nanoelectrode array structures (Fig. 1(a)). Such structures consist of drain and source electrodes with a buried local gate to use as ChemFET. The design includes two modifications with different electrode pairs separated by a constant spacing of 50 μm between them (Fig. 1(b)). The first modification consists of five pairs drain-source electrodes and the second contains nine pairs. The in-plane gap between drain and source electrodes was set to 3.5 μm, as this dimension proved ideal for the NWs alignment in our previous study [10]. The gate electrode with a width of 1.5 μm is locally placed between this gap formed by a SiO_2 trench (Fig. 1(c)). Each array is surrounded by circular gold stripes that serve as hydrophobic rings. These rings ensure the confinement of the droplet with suspended NWs on the electrode area during DEP (Fig. 1(d)) technique.

To fabricate these structures, EBL was first used to perform nanoelectrode arrays with a "clothespin" pattern. The red color in Fig. 1(c) represents the EBL pattern, and the yellow color is the remaining nanoelectrode ends created by the dry etching procedure. The nanoelectrode arrays contain electrode fingers with two different widths. Thus, the electrode fingers on the two left arrays have a width of 200 nm, whereas those on the right have a width of 300 nm (Fig. 1(a)). The entire electrode finger is 48 μm long and is divided into three parts. The first part corresponds to the triangularly shaped incoming microelectrodes connected to the middle electrode with a width of 1.5 μm. The last is finally connected to the nanoelectrode, which ends at the gate channel boundary (Fig. 1(c)).

Generally, the integration of the NWs and the number of aligned NWs across the faced nanoelectrodes in the array can be influenced by several factors, including the geometry and width of electrodes (which should be comparable to the NW diameter), DEP parameters, NWs concentration, and volume of droplets during DEP [21, 22]. In this work, we paid special attention to the reproducible integration of aligned SNW across the ChemFET nanoelectrodes, further improving our previous design of nanoelectrodes for chemoresistive operation [10]. Therefore, to achieve the alignment of SNW across the electrodes, we designed two dielectric shielding window structures based on a SiO_2 layer fabricated with atomic layer deposition (ALD): the wide one of 10 μm × 20 μm, and the narrow one of 200–300 nm × 10 μm. Figure 2 shows a schematic view of the dielectric shielding (alignment window) to favor the SNW interconnection.

2.2 Fabrication of ChemFET nanosensors platform

We fabricated the ChemFET arrays using standard surface microfabrication techniques such as thermal oxidation, ALD, reactive ion etching (RIE), and both EBL and ultraviolet (UV) lithography for dimensions lower or larger than 1 μm, respectively.

The fabrication process starts on a Si wafer with a diameter of ~ 100 mm thermally oxidized to form ~ 300 nm thick SiO_2 layer (Fig. 3(a)). The SiO_2 trenches are fabricated in the first step. To this end, we coated the wafer with a positive photoresist (PR) and then exposed it using UV lithography through a soda-lime mask employing mask aligner MA8 (Süss MicroTec, Switzerland). Then, we used a standard tetramethylammonium hydroxide (TMAH) based developer and performed descum using O_2 plasma. The SiO_2 was etched by RIE with Ar/CHF_3 gas mixture. Subsequently, we removed the PR in 1-methyl-2-pyrrolidinone (NMP) solution, rinsed the wafer with distilled water, and dried it with nitrogen steam.

The second step aimed to fabricate the gate electrode by lift-off

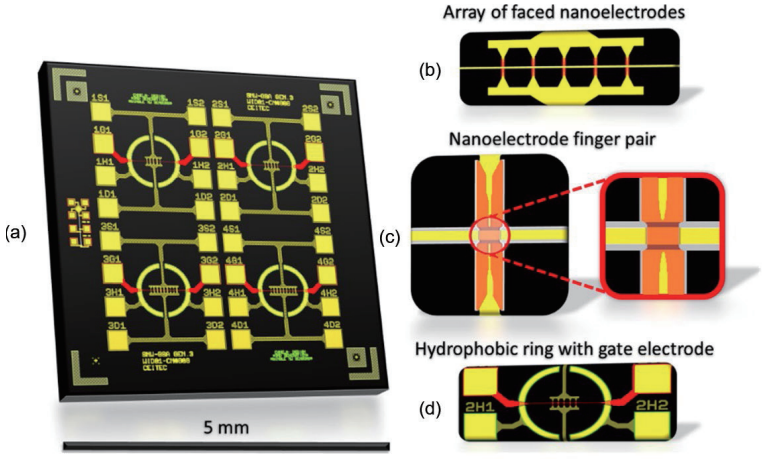

Figure 1 Chip design and layout of the functional blocks (yellow: microelectrodes and faced nanoelectrodes system (Au layer); orange: EBL pattern; black: thermal SiO_2 layer; red: the gate electrode; grey: channel for the gate electrode). (a) Detailed view of the full-size chip. (b) Array with five faced nanoelectrodes. (c) Detailed view of the nanoelectrode "clothespin" pattern at the crossings with the gate electrode. (d) Gold ring surrounding the array of nanoelectrodes and the gate electrode.

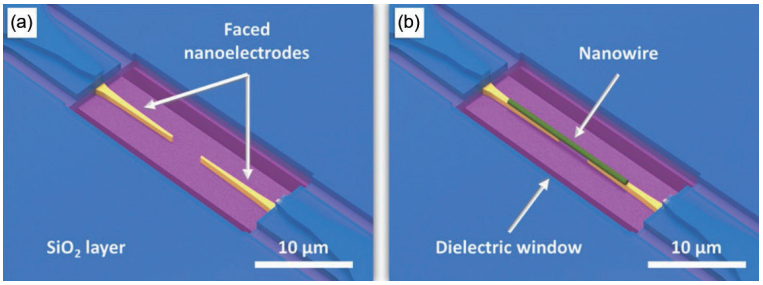

Figure 2 Illustration of the alignment dielectric (shielding) windows (a) before and (b) after integrating SNW by DEP.

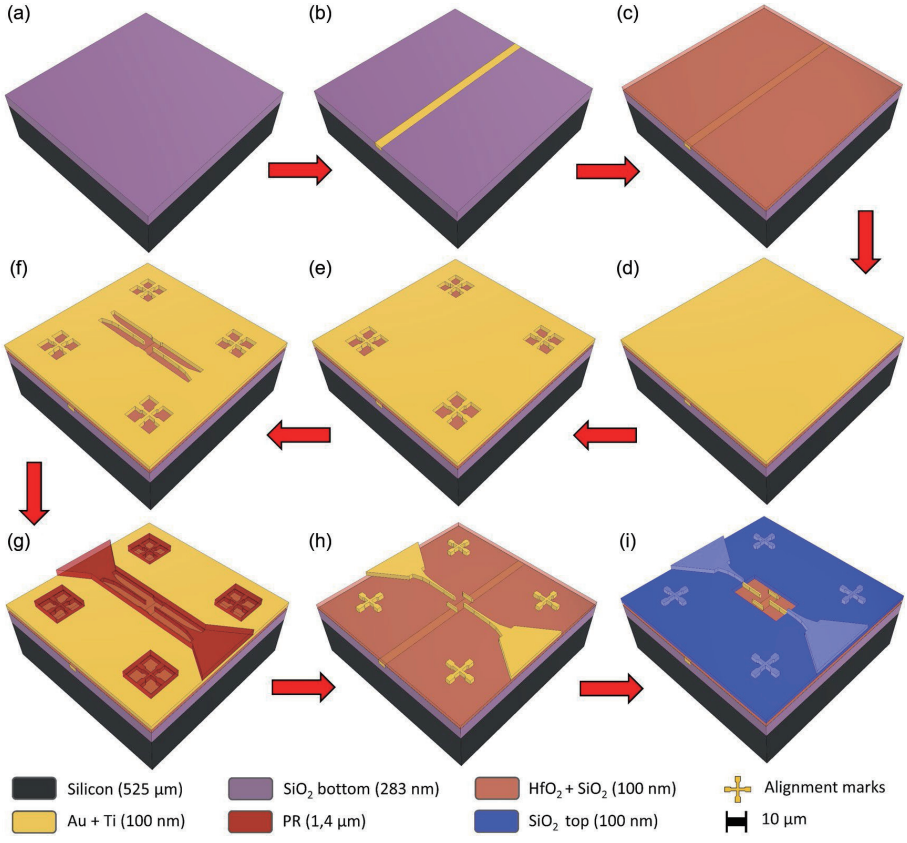

Figure 3 Schematic view of the chip fabrication process. (a) Si substrate with SiO_2 layer (thermal oxidation). (b) Buried gate electrode Ti/Au layer (e-beam evaporation). (c) Dielectric stack HfO_2 + SiO_2 layer (ALD deposition). (d) Ti/Au layer (e-beam evaporation). (e) EBL automatic calibration marks. (f) Faced nanoelectrodes (ion-milling). (g) Remaining electrode pattern fabrication (UV lithography). (h) Remaining electrode system linked to the faced nanoelectrodes after Au/Ti etching (ion-milling). (i) Wide window pattern created in SiO_2 layer (RIE).

process using a combination of bottom resist with standard positive PR. This process was performed as described above. Then, we deposited ~ 3 nm thick Ti as an adhesion layer and ~ 97 nm of Au using e-beam evaporator P397 (Bestec, Germany). Followingly, we removed the PR in NMP solution by placing the wafer upside-down to avoid the contamination caused by metal particles from the deposited layer on PR (Fig. 3(b)).

For the next step, we used ALD Fiji 200 system (Ultratech/Cambridge NanoTech, USA) to deposit the ~ 10 nm of HfO_2 and ~ 90 nm of SiO_2 that serve as gate dielectric stack (Fig. 3(c)). We also deposited a new Ti/Au stack over the dielectric stack with the same thickness as previously and spun the positive EBL resist, which was then exposed in e-beam writer Raith150 Two (Raith, Germany) (Figs. 3(d)–3(f)).

We used sophisticated tools to achieve high-resolution structures without distortion. A high-resolution EBL is severely impacted by process effects such as beam scattering effects (proximity) and tool implied artifact forming effects. Hence, we employed the GenISys Tracer® and Beamer® software that allow calibrating the exposition parameters by simulation for a specific resist type or thickness, taking into account the underlayer materials. These effects cause the nonideal pattern transfer by various error sources. We extracted dose distribution data (Fig. 4) from Beamer software, which calculates according to GenISys Tracer® monte-carlo simulations to obtain high-resolution shapes. The resulting proximity effect simulation for the faced nanoelectrodes is shown in Fig. 4.

Thus, we exposed only the small areas to create the sharp ends of electrodes with ~ 200 and ~ 300 nm widths. Followingly, we used amyl acetate-based developer to create a pattern for the subsequent ion-milling. We used ion-milling system (SCIA, Germany) equipped with Kaufman ion-beam source to remove the Au and Ti and stop on underneath SiO_2 layer. An ion-mass spectrometer controlled this process. Then, we removed EBL resist in NMP solution.

Additionally, we created the pattern which connects the conductive paths to previously shaped "clothespin" (Figs. 5(a) and 5(b)). This pattern made of Ti/Au stack layer was defined by UV lithography using a negative PR followed by exposure on MA8. We used the PGMA (2-methoxy-1-methylethyl acetate)-based developer recommended by the supplier for this PR. We then used ion-milling instrument as described before to remove the rest

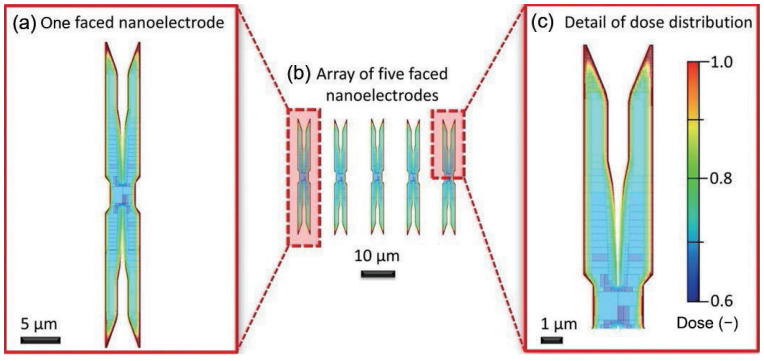

Figure 4 Illustration of EBL proximity effect simulation. (a) One faced nanoelectrode ("clothespin"), (b) array of five faced nanoelectrodes, and (c) detail of dose distribution with a dose scale bar.

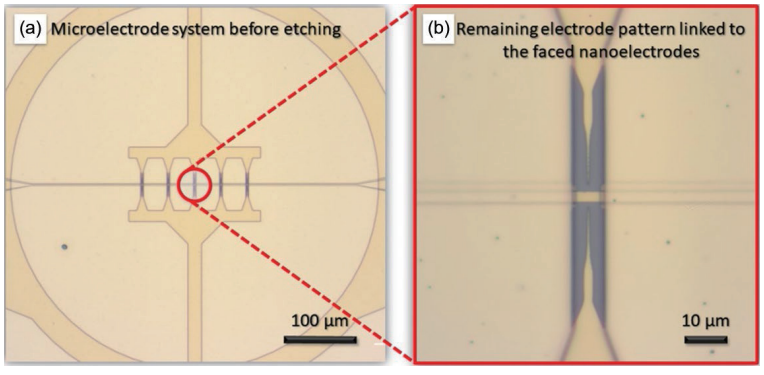

Figure 5 Connecting the remaining microelectrode system to the nanoelectrode array. (a) Microelectrode with a hydrophobic ring structure before etching. (b) Remaining electrode pattern linked to the faced nanoelectrodes.

of the Ti/Au layers. The PR was removed in NMP solution, and the wafer was rinsed by IPA and dried by nitrogen (Figs. 3(g) and 3(h)).

Finally, we performed the last deposition of ~ 100 nm thick SiO_2 layer using ALD. Such a layer forms the alignment windows that allow connecting the NWs between the faced nanoelectrodes during DEP, avoiding the connection with surrounding conductive paths (Fig. 3(i)). This step also allowed for opening the windows to the connection pads for wire bonding. As mentioned above, the design includes two types of windows. The wide window was formed using UV lithography employing the same positive PR as the first step. The narrow window was additionally shaped by EBL to achieve a small alignment window. We etched the SiO_2 layer in RIE instrument with Ar/CHF_3 plasma.

To finalize the whole process, the wafer was covered by positive PR as a protective layer and then diced using a saw into single chips with a size of ~ 5 mm × 5 mm.

2.3 Nanowire synthesis and characteristics

Tungsten oxide NWs were synthesized at ~ 390 °C on small Si wafer tiles (~ 2 mm × 2 mm) to facilitate the subsequent steps, including the dispersion of nanowires and DEP. The NWs were synthesized without catalyst seeds using Aerosol-Assisted Chemical Vapor Deposition (AACVD) method. The precursor solution consisted of a mixture of 5 mL of methanol (Penta, ≥ 99.8 %) and 20 mg of $W(CO)_6$ (Sigma-Aldrich, ≥ 97 %). This solution was atomized using a piezoelectric ultrasonic atomizer (Johson Matthey Liquifog) and delivered to the reaction zone using N_2 flow as carrier gas. Further details of the process and equipment are described elsewhere [23, 24]. The structures synthesized by this method display NW-like morphology with diameters and lengths of ~ 100 nm and ~ 10 μm, respectively, as shown in the scanning electron microscope (SEM) image in Fig. 6(a). The NWs are crystalline, showing highly ordered lattices by high-resolution transmission electron microscopy (HRTEM) (Fig. 6(b)) with a spacing distance (d) of ~ 3.5 Å. X-ray diffraction analysis of these films using Bragg-Brentano setup generally displayed intense diffraction peaks at 23.5° and 48.2°, corresponding to the 020 and second-order 040 diffractions of a monoclinic P21/n space group tungsten oxide (ICCD card no. 72-0677) as resolved previously [25]. This indicates a preferred orientation of the NWs in the (010) direction over the substrate, which is consistent with the planar spacing in the growth direction found by HRTEM. The inset in Fig. 6(b) shows the typical diffraction pattern recorded for the NWs. XPS of the nanowire displayed typical W $4f_{7/2}$, W $4f_{5/2}$, and W $5p_{3/2}$ XPS core level peaks (Fig. 7, the adventitious C 1s peak located at 284.3 eV was used to calibrate the spectra), in agreement with previous reports on tungsten oxide nanowires synthesized via AACVD [26]. Two doublets were needed to fit the W4f core level spectrum. The main doublet peak at 35.4 eV is associated to the tungsten atoms with oxidation state of +6 from WO_3, whereas the second doublet peak at 34.3 eV relates to the presence of tungsten atoms with oxidation state lower than +6, suggesting the presence of sub-stochiometric tungsten oxide (WO_{3-x}). The spectrum also displays a small component centered at 41.2 eV assigned to the W $5p_{3/2}$ core level spectrum.

2.4 Sensor assembling and NWs integration by DEP process

We used a TO-8 package of a soldered custom-made Al_2O_3 ceramic substrate with an isolated Pt heater fabricated using thick-film technology as a chip holder. Then we used thermal conductive paste Epotek H31D (Epoxy technology, USA) to stick the chip on the alumina (Al_2O_3) substrate. We made electrical connections between the chip and TO-8 package using wire-bonding method. The assembly structure was then placed into a printed circuit board connected to a waveform generator for the DEP procedure.

We detached the NWs from the Si tiles by immersing and sonicating them using SONOREX-Digital 10P (Bandelin,

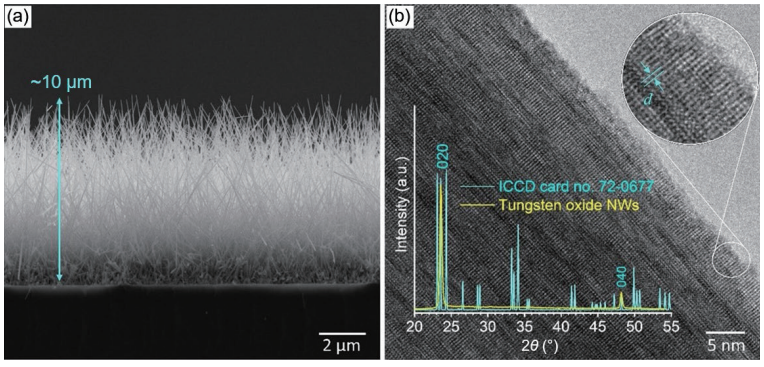

Figure 6 (a) Cross-section SEM image of the as-deposited NWs on Si substrate, and (b) HRTEM of a SNW showing in the insets of the interplanar spacings and the X-ray diffraction pattern of the NWs.

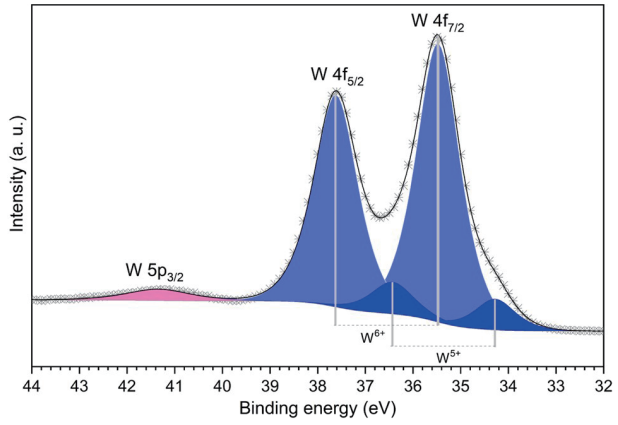

Figure 7 XPS core levels of the AACVD deposited nanowires showing the W 4f levels for stochiometric WO_3 (light blue colour) and sub-stochiometric WO_{3-x} (blue colour).

Germany) for ~ 10 s in a beaker with ~ 1 mL of deionized (DI) H_2O. DI H_2O is a polar medium with high permittivity and low evaporation coefficient that has proved better suitability for DEP process in comparison to volatile liquids such as isopropyl alcohol, methanol, ethanol, or acetone [22]. The DI H_2O solution containing the dispersed NWs was placed into a ~ 3 mL syringe connected to a contact angle measurement station Phoenix 300 (SEO, South Korea) equipped with charge coupled device (CCD) cameras (Fig. 8(a)). Then, a droplet with a volume of ~ 5 μL of the solution was deposited over the chip while connected to a waveform generator 33220A (Agilent, USA). This instrument generated an AC sine wave signal with peak-to-peak voltage of ~ 2.5 V with no DC offset at a frequency of ~ 9.5 MHz for ~ 120 s to align the SNW between the electrode pairs by dielectrophoretic forces. After a few seconds of the DEP process running, the droplet was dried by N_2 flow. Figure 8(b) shows an example of a pair of nanoelectrodes after integrating the nanowires.

2.5 Electrical and gas sensing characterization

The behavior of the ChemFET's nanowire channel under the influence of sweeping gate voltage potential was measured in air at room temperature (RT) using a probe station MPS150 (Cascade Microtech, USA) connected to the parameter analyzer 4200-SCS (Keithley, USA). We used four-wire Kelvin arrangement to ensure the correct readout of drain-source voltage (V_{DS}) and drain current (I_{DS}), neutralizing the effect of probes and conductors. The ChemFET's output characteristics were obtained using common tests for MOSFET devices from the project library of the parameter analyzer's software Clarius (Tektronix, USA), which offers many pre-programmed characterization tests for various device measurements. Specifically, output characteristics were performed by sweeping the drain-source voltage (V_{DS} = ± 20 V), keeping constant gate voltage (V_G) while measuring drain current (I_{DS}) flowing through the NW channel, whereas the transfer characteristics were recorded by keeping the V_{DS} constant when sweeping the (V_G = ± 10 V) and measuring the channel current (I_{DS}) conductivity changes. The measured drain current (I_{DS}) flowing through the NW channel was limited to 120 nA (I_{DSmax} = 120 nA) to prevent damaging the NWs for both characterization tests.

The tests were performed in a custom-made gas station system equipped with three mass-flow controllers (MFCs) for precise gas flow adjustment in a range from ~ 1 mL·min^{-1} to ~ 2000 mL·min^{-1}. The whole system is controlled by LabVIEW software, which allows the setting of automatically controlled measurement procedures and controls the MFCs, solenoid valves, stepper motor, and electronics for measurement. We used a source meter unit SMU 2450 (Keithley, USA) for the resistance measurement, and SMU 2401 (Keithley, USA) for gate voltage setting (V_G). For the heater, we employed a voltage source 3633A (Agilent, USA) controlled by a feedback loop and a calibrated temperature sensor Au 220 monitored by a multimeter 33410A (Agilent, USA). We

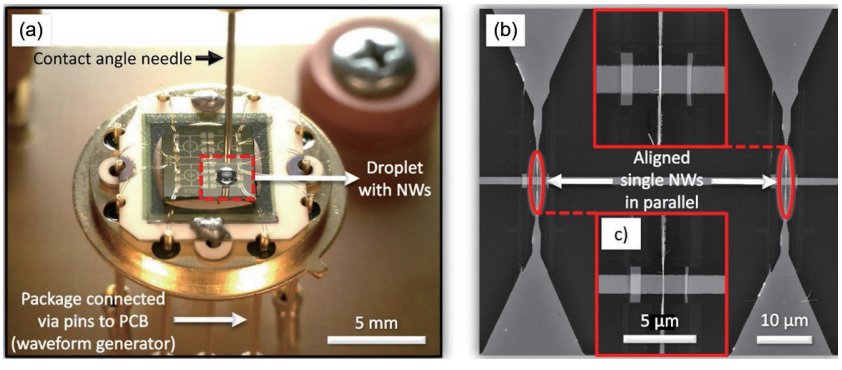

Figure 8 (a) Photograph of the chip and the drop containing the suspended nanowires ready for the DEP step. (b) View of the aligned SNWs integrated across the faced nanoelectrodes after DEP process. (c) Detailed view on a SNW between an electrode pair.

also used a power supply U3606A (Agilent, USA) to control the chamber heating system.

The assembled ChemFET was validated by testing the structures at various temperatures (T) ranging from RT ~ 22 to ~ 200 °C and towards H_2 and NO_2 due to tungsten oxide sensitivity to this gaseous analyte [25]. The sensor response (S_R) was defined as $[(R_{air}/R_{gas}) \times 100]$ for H_2 (reducing gas) and $[(R_{gas}/R_{air}) \times 100]$ for NO_2 (oxidizing gas), where R_{air} is the sensor resistance in air at the stationary state and R_{gas} is the sensor resistance after thirty minutes of analyte exposure. The response time (t_{resp}) was defined as the time required to reach 90% of the sensor response. Also, we explored the influence of the gate voltage (V_G) changes on the sensitivity to H_2 gas while monitoring the electrical resistance of the tungsten oxide SNWs between the drain and source electrodes and applying different I_{DS}. The isothermal measurements were performed using a constant I_{DS} and several cycles with different V_G. Each cycle included a stabilization period, response and recovery time equally long. The measurement cycle started with the V_G of 0 V and continued with different V_G in the following order of –5 and 5 V.

3 Results and discussion

The test and results of the assembled structures focussed on three aspects related to (1) the influence of the dielectric window size on the integration of SNWs by DEP process, (2) the influence of the gate voltage bias on the electrical properties of the SNW ChemFET channel and (3) the validation of the SNW ChemFET structure as a gas sensor.

3.1 Influence of dielectric window size

Figure 9 shows the surface topography mapping of the two types of fabricated dielectric windows recorded by atomic force microscopy (AFM) in ScanAsyst® mode. These images evidence the difference between the wide (Fig. 9(a)) and narrow modifications (Fig. 9(b)). The green-colored surface shows the SiO_2 shielding layer, whereas the surface in yellow or orange displays the areas in which the gold layer was patterned. The opened windows, both wide and narrow, are displayed in dark blue color.

Both window structures were tested for the integration of NWs by DEP process. Results in Fig. 10 show the SEM images of the structures after DEP and the significant difference between the number of captured NWs in both windows. One can notice from these results that the wide window holds bunches of multiple randomly connected NWs (MNWs) (Fig. 10(a)). In contrast, the narrow window facilitates the integration of SNW, allowing a good alignment of the NW between electrodes (Fig. 10(b)). These results indicate that despite the more complex fabrication process required to structure the narrow windows, such structures are well-suitable to limit the number of connected NWs to only SNW between the faced nanoelectrodes (Fig. 10(c)). While the electrode geometry is a key factor for the precise integration of one-dimensional structures, as demonstrated in previous reports [10, 27, 28], our results also indicate that the incorporation of shielding windows with similar dimensions to those of the NWs are more convenient for the NW integration process. Previously, we experimentally determined the most convenient nanoelectrode geometry for the AACVD tungsten nanowires. These structures allowed for integrating single nanowires in an array of nanoelectrodes with a success rate of approximately 33% [10]. The present system incorporating the shielding nanowindows showed a similar success rate. However, it added advantages compared to the previous system, including a better alignment of the NWs, and avoiding their aggregation along and across the faced nanoelectrodes, as shown in Fig. 10(a).

Therefore, we used the narrow dielectric window structures to study further the SNW-based ChemFET gas sensors. Further analysis of these structures by AFM also demonstrates the integration of the wire, and its contact with the nanoelectrodes suggests that the NWs are flexible and attempt to reproduce the surface topography in the window (Fig. 11).

3.2 Electrical properties of ChemFET structure

The output characteristics of the ChemFET using a constant gate voltage V_G (from –6 to 6 V with steps of 1 V) and varying the drain to source voltage V_{DS} (from 0 to 3 V) are shown in Fig. 12(a).

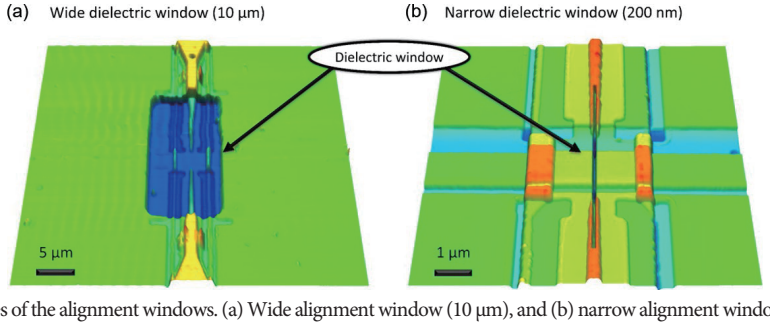

Figure 9 AFM topography images of the alignment windows. (a) Wide alignment window (10 μm), and (b) narrow alignment window (200 nm).

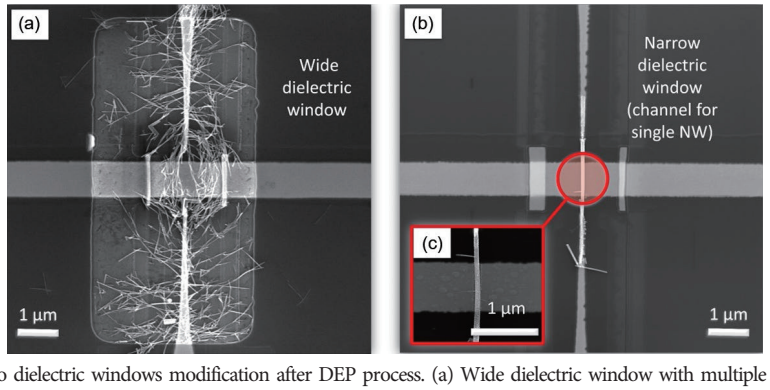

Figure 10 SEM inspection of two dielectric windows modification after DEP process. (a) Wide dielectric window with multiple interconnected NWs. (b) Narrow dielectric window with SNW interconnection. (c) Detail of SNW aligned within the window channel.

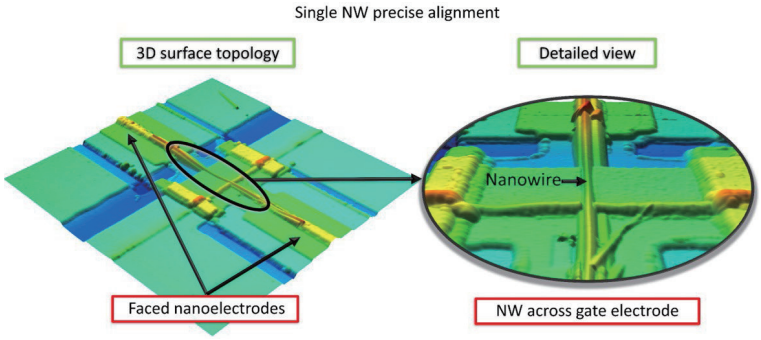

Figure 11 Detailed 3D surface topography obtained by AFM (15 μm × 15 μm) showing an aligned SNW inside the narrow dielectric window and across the gate electrode.

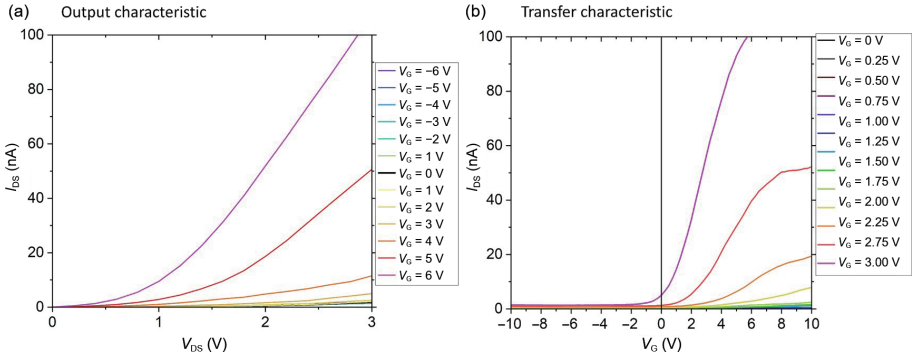

Figure 12 (a) Output, and (b) transfer characteristic of the nanowire channel of the ChemFET structure.

Significant enhancement of the current density through the channel is particularly noticeable at gate bias voltage above V_G = 3 V. For example, when we applied a drain to source voltage V_{DS} of 3 V and gate voltage V_G of 6 V (see the output characteristic curve), the drain current I_{DS} is two times higher (I_{DS} > 100 nA) than the drain current I_{DS} recorded for a gate voltage V_G of 5 V (I_{DS} ~ 50 nA) applied at the same drain to source voltage (V_{DS} = 3 V). Results in Fig. 12a demonstrate that the drain current (I_{DS}) flowing through the nanowire channel has a direct proportional increase to the positive increments of the gate voltage (V_G) and the drain to source bias V_{DS} is in agreement with previous literature [29]. In contrast, the negative gate bias tends to close the channel, and drop the drain current I_{DS}. The influence of the gate bias on the switching properties (ON and OFF) of the drain current I_{DS} is better interpreted by evaluating the transfer characteristic displayed in Fig. 12(b). The transfer characteristic was measured at a constant drain to source voltage V_{DS} (from 0 to 3.5 V) with steps of 0.25 V and varying the gate voltage V_G from −10 to 10 V. The influence of the gate voltage V_G on the channel's drain current I_{DS} can be observed in Fig. 12(b). Results show that positive gate biases lead to higher NW channel conductivity, especially when applying a drain to source voltage V_{DS} of 3 V. In contrast, negative gate biases generally deplete of charge carriers in the NW channel diminishing the conductivity through it. However, this behavior depends partly on the drain to source voltage V_{DS}. Thus, we observed that when the drain to source voltage V_{DS} reaches a certain level, for example: for V_{DS} = 3 V, the negative gate bias is unable to keep the channel closed, showing a small drain current I_{DS} as the gate voltage V_G changes from 0 to −2 V approximately. Despite this, the transfer characteristic clearly shows the switching behavior of the SNW-based ChemFET channel and exhibits the control of the gate bias V_G on drain current I_{DS} by opening or closing the conduction channel as the gate bias V_G passes from positive to negative bias.

The observed output and transfer characteristics prove the presence of a n-type channel material integrated across the faced nanoelectrodes, similar to other reports on NW FET structures in the literatures [30, 31]. The following section describes the gas sensing properties and mechanism of detection in this type of structures with more details.

3.3 Gas sensing characterization

To evaluate the gas sensing properties of the ChemFETs, we tested the influence of various parameters, including the operating temperature, gate voltage, and drain current. The baseline resistances remained at stable values during the whole measurement. The assembled ChemFET structures were validated to reducing (H_2) and oxidizing (NO_2) gases at 200 °C, as this temperature was found to deliver the maximum responses to these analytes, in agreement with our previous evaluations for tungsten oxide SNWs [10]. The measurement of the baseline resistance in air (R_{air}) towards different drain-source currents (I_{DS}) displayed an inverse dependence of the R_{air} to I_{DS}, showing a R_{air} saturation point for drain-source currents above 20 nA. Results in Fig. 13 also show the dependency of R_{air} on V_G, showing a noticeable increase of the SNW's resistance as the V_G changes from 0 V to negative bias. This is consistent with the literature and attributed to the withdrawal of electrons from the n-type tungsten oxide NW, which narrows the conduction channel (D_{cond}) and increases the wire's electrical resistance [32].

In contrast, when V_G changes from 0 V to positive bias, the NW's resistance decreases, suggesting a nonlinear behavior for the conductivity. This is also in agreement with other ChemFET gas sensors in the literatures [32–34], and it is believed to occur due to the saturation of the electron density in the NW channel [32]. The inset in Fig. 13 illustrates this phenomenon by showing the widening and narrowing of the NW conduction channel as V_G changes from positive to negative bias, respectively.

Measurements of the NW response (S_R) to H_2 and NO_2 revealed a different tendency concerning the V_G for each gas (Fig. 14). For instance, results for H_2 showed an improvement of the response by applying negative V_G instead of positive, whereas results for NO_2 indicated a soft diminution of the response as a function of the positive and negative V_G. Overall, results show a

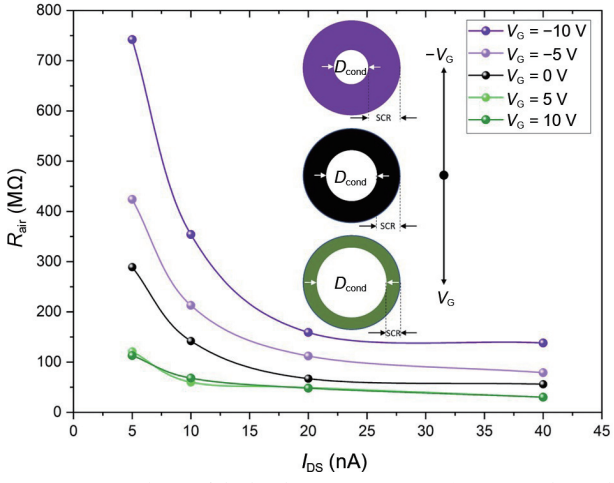

Figure 13 Dependency of the baseline resistance (in air) on V_G and I_{DS}. The inset illustrates the effect of V_G on the NW conduction channel (D_{cond}).

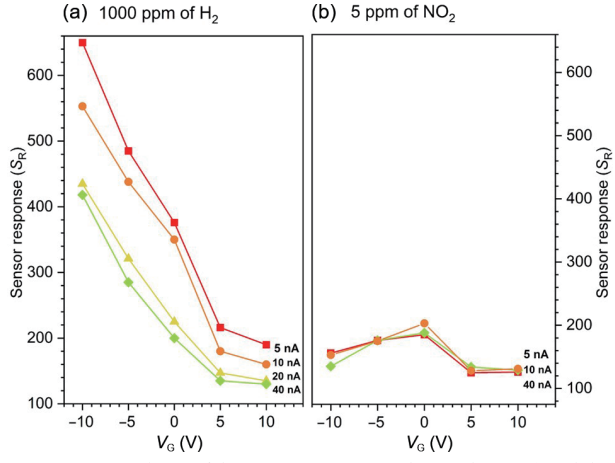

Figure 14 Dependency of the sensor response on the gate bias (V_G) and drain current (I_{DS}) in the presence of (a) 1000 ppm of H_2, and (b) 5 ppm of NO_2.

similar tendency, regardless of the I_{DS} applied, displaying greater response magnitudes for an I_{DS} of 5 nA than that of 10, 20, or 40 nA in the case of H_2. The sensor response became noisy and unstable for some of the measurements as V_G reached −10 V, suggesting these conditions are close to the operation limit of the ChemFET structure when working at a high temperature (200 °C). Figure 15(a) displays the influence of the response time (t_{resp}) towards V_G, showing an improvement of the response dynamics to H_2 for negative V_G. Better response dynamics were also noticed for NO_2 by operating the sensor in ChemFET with both positive and negative V_G. Moreover, the tests to different concentrations of H_2 showed proportional changes with the concentrations, suggesting a linear behavior (Fig. 15(b)).

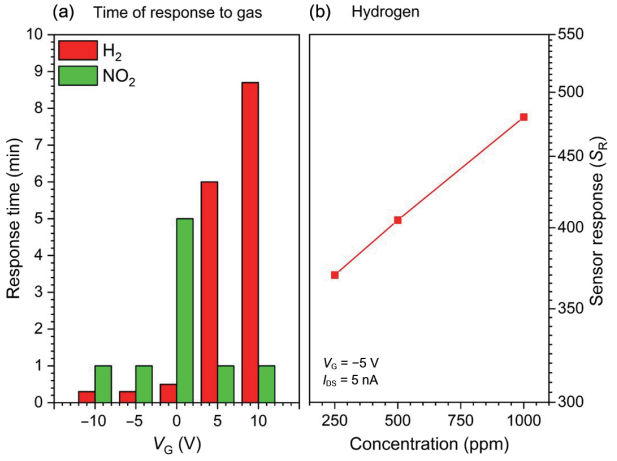

Figure 15 (a) Response time of ChemFET to H_2 (1000 ppm) and NO_2 (5 ppm). (b) Dependency of the response on different H_2 concentrations.

Figure 16 compares the typical responses to hydrogen and nitrogen dioxide recorded on the ChemFET sensors for V_G of 0 and ±5 V. The responses corroborate the n-type semiconductor behavior of the tungsten oxide NWs, showing a decrease of the electrical resistance towards hydrogen (reducing gas), and reversely an increase of the electrical resistance towards nitrogen dioxide (oxidizing gas).

The response magnitudes of the ChemFET are also comparable or better than other nanowire-based gas sensors in the literatures (Table 1), including those based on multiple nanowires (M-NWs). The single nanowire arrays (S-NWA) evaluated here also show better response time (e.g., to H_2, 20 s) compared to previous chemoresistive sensors based on multiple nanowires (290 s) [25]. Overall, results suggest that the ChemFET structures are good at improving the sensor response and the time of response (particularly to H_2) with respect to resistive sensors based on single or multiple nanowires. It is worth noticing, though, that these comparisons represent only an approximation of the quality of the sensors as their performance generally depends on a variety of other parameters, including the sensing material, sensor architecture, and test parameters.

Figure 17 illustrates the effect of the reducing and oxidizing gases on the conduction channel of the semiconducting wires after the air pre-adsorption cycle. The illustration depicts how the initial change of the baseline resistance (observed both in Figs. 16 and 17) has a strong influence on the magnitude of response as a function of applied V_G. This is noticed particularly for the reducing analyte, which shows a response dominated by the V_G dependant conductivity changes in the pre-adsorption stage rather than hydrogen exposure (the resistance in hydrogen shows a non-dependant behavior concerning applied V_G, Fig. 16(a)). This is also observed for the oxidizing gas, although at lower proportion,

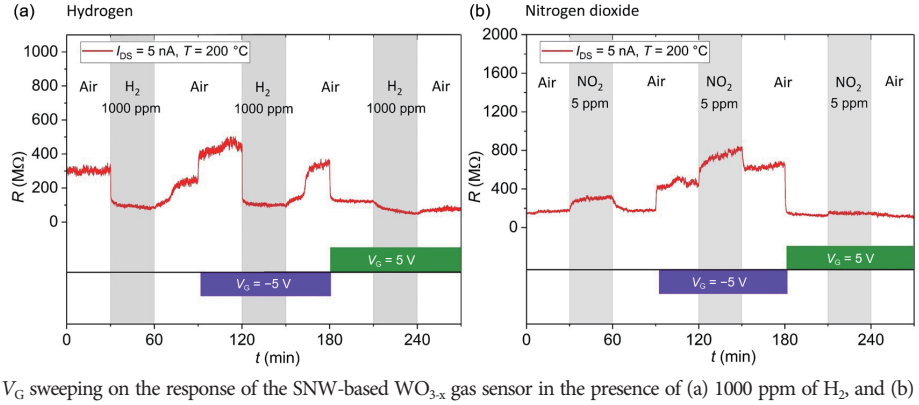

Figure 16 Effect of the V_G sweeping on the response of the SNW-based WO_{3-x} gas sensor in the presence of (a) 1000 ppm of H_2, and (b) 5 ppm of NO_2 measured both at the same temperature of 200 °C and constant current I_{DS} = 5 nA.

Table 1 Comparative table displaying the response and recovery times recorded in this work and the literatures towards H_2 and NO_2

Structures	Material	Operation principle	Gas	S_R(%)	t_{resp} (s)	T(°C)	Concentration ppm	Reference
S-NWA	WO_{3-x}	FET (V_G = −10V)	H_2	650	20	200	1000	This work
S-NW	SnO_2	Resistive	H_2	342	20	200	500	[35]
M-NWs	WO_{3-x}	Resistive	H_2	450	290	250	500	[25]
M-NWs	SnO_2	Resistive	H_2	140	35	210	400	[36]
S-NWA	WO_{3-x}	FET (V_G = −10V)	NO_2	156	60	200	5	This work
S-NWA	WO_{3-x}	Resistive	NO_2	248	360	250	5	[10]
S-NW	ITO	Resistive	NO_2	108	60	200	5	[37]
M-NWA	ZnO	Resistive	NO_2	250	140	~ 160	5	[38]

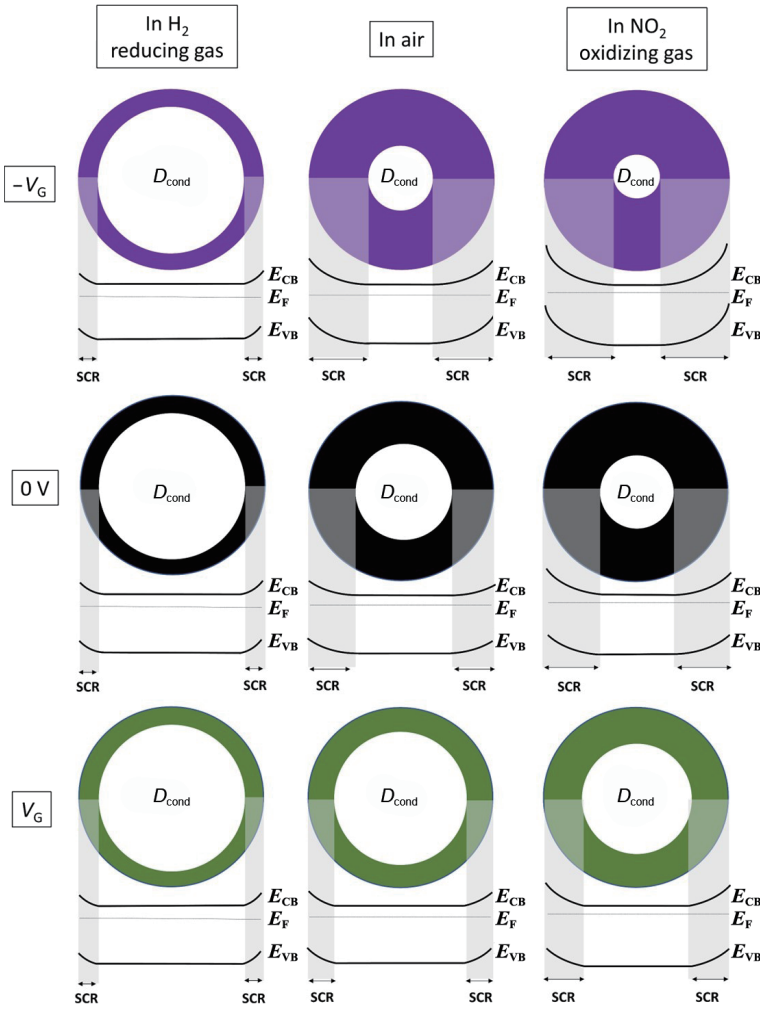

Figure 17 Illustration of the gas sensing mechanism, and the influence of the gate voltage (V_G) and gas type on the conduction channel of the gas-sensitive NW (cross-sectional view). D_{cond} is the diameter of the non-depleted region available for charge conduction through the NW, E_{CB} is the conduction band minimum, E_F is the Fermi level, E_{VB} is the valence band maximum, and SCR represents the space charge region at the NW surface (not to scale).

as both air and NO_2 have similar effects on the wire surface. This is because (regardless of the conductivity type of the sensing material) the oxidizing gases withdraw electrons from the conductive channel and the material becomes depleted of electrons. In contrast, reducing gases donate electrons to the sensing material [10]. This is the reason why the response of the n-type ChemFET does not show significant improvement to NO_2 compared to the resistive mode (V_G = 0 V). To favor the response to oxidizing gases, p-type sensing materials are suggested [31].

Figure 14 corroborates and summarizes this statement by showing that the main contribution to the ChemFET response upon H_2 occurs in the subthreshold regime, particularly under conditions when the negative gate bias is applied and the NW channel is almost closed, in agreement with other reports in the literatures dealing with NW ChemFET sensors [39, 40].

Overall, results indicate that the sensor response to reducing gases is especially influenced by the changes of the baseline resistance in the preabsorbed state (in air) induced by the gate voltage (Fig. 17). Also, the tests show that the responses to H_2 increase by setting a low drain current through the NW channel, i.e., by operating the ChemFET in the subthreshold regime.

The results above validate the functionality of the ChemFET sensor array, showing consistent behavior with previous single ChemFET sensors based on n-type semiconductors towards reducing and oxidizing gases. Such a sensing device, which includes other complementary nanoelectrode arrays in the same

chip, could favor the selectivity of gas sensors by introducing sensing structures (i.e., conduction channels) with different characteristics. Using one type of semiconductor is not beneficial in distinguishing the types of gases as long as no metal-oxide material is exclusively selective for a given analyte. In this context, the design and fabrication methods showed in this work may be an attractive route for developing the next generation of e-nose based on ChemFET gas sensors operating with single gas-sensitive nanowires.

4 Conclusions

This work described and discussed the design, fabrication, and functionality of ChemFET nanosensor arrays based on SNWs. The fabrication of these new structures exploited the use of micro and nanofabrication techniques combining both UV and e-beam lithography and adding unique processing steps for building ChemFET array structures (taking further the processes we previously developed for chemoresistive sensors [10]). The new structures improved the selective integration of SNWs due to each element of the ChemFET array containing shielding nanoscale windows (200–300 nm) adapted to the diameter of the SNW (100 nm). The SNW-based ChemFET array's output and transfer characteristics demonstrated the gate bias role in regulating the drain current. These properties allowed the structures to operate as stable ChemFET gas detectors registering low deviations of the baseline resistance during the tests. Overall, results proved the possibility of tuning the response of the SNWs by modulating the applied voltage gate and drain current, demonstrated improved characteristics to H_2 when the ChemFET operates in the subthreshold regime. The new structure and methods proposed for fabricating SNW-based ChemFET arrays proved to be versatile, reproducible, and most likely capable of adapting to other systems where SNW arrays are required.

Acknowledgements

This work was supported by the Czech Science Foundation (GAČR, No. 22-14886S), and the MCIN/AEI/10.13039/501100011033 (No. PID2019-107697RB-C42 (ERDF A way of making Europe)).

Conflict of Interest

The authors declare no conflict of interest.

Author Contributions

O. C. conceived of the presented idea, run experiments, and wrote the manuscript with support from I. G. and J. B. J. S. contributed to the chip design and fabrication. S. V. wrote and revised the manuscript, and got the funding for realizing this work. All authors provided critical feedback and discussed the results to the final manuscript.

Funding note: Open access publishing supported by the National Technical Library in Prague.

References

[1] Miller, D. R.; Akbar, S. A.; Morris, P. A. Nanoscale metal oxide-based heterojunctions for gas sensing: A review. *Sens. Actuat. B Chem.* **2014**, *204*, 250–272.

[2] Liu, L.; Wang, Y. Y.; Liu, Y. H.; Wang, S. Q.; Li, T.; Feng, S. M.; Qin, S. J.; Zhang, T. Heteronanostructural metal oxide-based gas microsensors. *Microsyst. Nanoeng.* **2022**, *8*, 85.

[3] Gurlo, A. Nanosensors: Towards morphological control of gas sensing activity. *SnO_2, In_2O_3, ZnO and WO_3 case studies. Nanoscale* **2011**, *3*, 154–165.

[4] Gao, W. Y.; Zdrachek, E.; Xie, X. J.; Bakker, E. A solid-state reference electrode based on a self-referencing pulstrode. *Angew. Chem., Int. Ed.* **2020**, *132*, 2314–2318.

[5] Zhai, J. Y.; Yuan, D. J.; Xie, X. J. Ionophore-based ion-selective electrodes: Signal transduction and amplification from potentiometry. *Sens. Diagn.* **2022**, *1*, 213–221.

[6] Kaisti, M. Detection principles of biological and chemical FET sensors. *Biosens. Bioelectron.* **2017**, *98*, 437–448.

[7] Chartuprayoon, N.; Zhang, M. L.; Bosze, W.; Choa, Y. H.; Myung, N. V. One-dimensional nanostructures based bio-detection. *Biosens. Bioelectron.* **2015**, *63*, 432–443.

[8] Lu, Z. C.; Zhou, H.; Wang, Y.; Liu, Y. X.; Li, T. A controllable fabrication improved silicon nanowire array sensor on (111) SOI for accurate bio-analysis application. *Nano Res.* **2022**, *15*, 7468–7475.

[9] Zou, X. M.; Wang, J. L.; Liu, X. Q.; Wang, C. L.; Jiang, Y.; Wang, Y.; Xiao, X. H.; Ho, J. C.; Li, J. C.; Jiang, C. Z. et al. Rational design of sub-parts per million specific gas sensors array based on metal nanoparticles decorated nanowire enhancement-mode transistors. *Nano Lett.* **2013**, *13*, 3287–3292.

[10] Chmela, O.; Sadílek, J.; Domènech-Gil, G.; Samà, J.; Somer, J.; Mohan, R.; Romano-Rodriguez, A.; Hubálek, J.; Vallejos, S. Selectively arranged single-wire based nanosensor array systems for gas monitoring. *Nanoscale* **2018**, *10*, 9087–9096.

[11] Vallejos, S.; Grácia, I.; Chmela, O.; Figueras, E.; Hubálek, J.; Cané, C. Chemoresistive micromachined gas sensors based on functionalized metal oxide nanowires: Performance and reliability. *Sens. Actuat. B Chem.* **2016**, *235*, 525–534.

[12] Brunet, E.; Maier, T.; Mutinati, G. C.; Steinhauer, S.; Köck, A.; Gspan, C.; Grogger, W. Comparison of the gas sensing performance of SnO_2 thin film and SnO_2 nanowire sensors. *Sens. Actuat. B Chem.* **2012**, *165*, 110–118.

[13] Chen, X. P.; Wong, C. K. Y.; Yuan, C. A.; Zhang, G. Q. Nanowire-based gas sensors. *Sens. Actuat. B Chem.* **2013**, *177*, 178–195.

[14] Penner, R. M. Chemical sensing with nanowires. *Annu. Rev. Anal. Chem.* **2012**, *5*, 461–485.

[15] Ramgir, N. S.; Yang, Y.; Zacharias, M. Nanowire-based sensors. *Small* **2010**, *6*, 1705–1722.

[16] Hernández-Ramírez, F.; Tarancón, A.; Casals, O.; Rodríguez, J.; Romano-Rodríguez, A.; Morante, J. R.; Barth, S.; Mathur, S.; Choi, T. Y.; Poulikakos, D. et al. Fabrication and electrical characterization of circuits based on individual tin oxide nanowires. *Nanotechnology* **2006**, *17*, 5577–5583.

[17] Domènech-Gil, G.; Barth, S.; Samà, J.; Pellegrino, P.; Gràcia, I.; Cané, C.; Romano-Rodriguez, A. Gas sensors based on individual indium oxide nanowire. *Sens. Actuat. B Chem.* **2017**, *238*, 447–454.

[18] Wang, M. C. P.; Gates, B. D. Directed assembly of nanowires. *Mater. Today* **2009**, *12*, 34–43.

[19] Burg, B. R.; Poulikakos, D. Large-scale integration of single-walled carbon nanotubes and graphene into sensors and devices using dielectrophoresis: A review. *J. Mater. Res.* **2011**, *26*, 2123.

[20] Smith, B. D.; Mayer, T. S.; Keating, C. D. Deterministic assembly of

functional nanostructures using nonuniform electric fields. *Annu. Rev. Phys. Chem.* **2012**, *63*, 241–263.

[21] Raychaudhuri, S.; Dayeh, S. A.; Wang, D. L.; Yu, E. T. Precise semiconductor nanowire placement through dielectrophoresis. *Nano Lett.* **2009**, *9*, 2260–2266.

[22] Maijenburg, A. W.; Maas, M. G.; Rodijk, E. J. B.; Ahmed, W.; Kooij, E. S.; Carlen, E. T.; Blank, D. H. A.; Ten Elshof, J. E. Dielectrophoretic alignment of metal and metal oxide nanowires and nanotubes: A universal set of parameters for bridging prepatterned microelectrodes. *J. Colloid Interface Sci.* **2011**, *355*, 486–493.

[23] Vallejos, S.; Gràcia, I.; Figueras, E.; Cané, C. Catalyst-free vapor-phase method for direct integration of gas sensing nanostructures with polymeric transducing platforms. *J. Nanomater.* **2014**, *2014*, 932129.

[24] Vallejos, S.; Pizúrová, N.; Čechal, J.; Gràcia, I.; Cané, C. Aerosol-assisted chemical vapor deposition of metal oxide structures: Zinc oxide rods. *J. Vis. Exp.* **2017**, *127*, 56127.

[25] Vallejos, S.; Umek, P.; Stoycheva, T.; Annanouch, F.; Llobet, E.; Correig, X.; De Marco, P.; Bittencourt, C.; Blackman, C. Single-step deposition of au- and pt-nanoparticle-functionalized tungsten oxide nanoneedles synthesized via aerosol-assisted CVD, and used for fabrication of selective gas microsensor arrays. *Adv. Funct. Mater.* **2013**, *23*, 1313–1322.

[26] Navío, C.; Vallejos, S.; Stoycheva, T.; Llobet, E.; Correig, X.; Snyders, R.; Blackman, C.; Umek, P.; Ke, X. X.; Van Tendeloo, G. et al. Gold clusters on WO_3 nanoneedles grown via AACVD: XPS and TEM studies. *Mater. Chem. Phys.* **2012**, *134*, 809–813.

[27] Xu, D. D.; Subramanian, A.; Dong, L. X.; Nelson, B. J. Shaping nanoelectrodes for high-precision dielectrophoretic assembly of carbon nanotubes. *IEEE Trans. Nanotechnol.* **2009**, *8*, 449–456.

[28] Montemurro, D.; Stornaiuolo, D.; Massarotti, D.; Ercolani, D.; Sorba, L.; Beltram, F.; Tafuri, F.; Roddaro, S. Suspended InAs nanowire Josephson junctions assembled via dielectrophoresis. *Nanotechnology* **2015**, *26*, 385302.

[29] Huo, J. P.; Zou, G. S.; Lin, L. C.; Wang, K. H.; Xing, S. L.; Zhao, G. L.; Liu, L.; Zhou, Y. N. Highly focused femtosecond laser directed selective boron doping in single SiC nanowire device for n-p conversion. *Appl. Phys. Lett.* **2019**, *115*, 133104.

[30] Jakhar, A.; Dhyani, V.; Das, S. Room temperature terahertz detector based on single silicon nanowire junctionless transistor with high detectivity. *Semicond. Sci. Technol.* **2020**, *35*, 125020.

[31] Han, J. W.; Rim, T.; Baek, C. K.; Meyyappan, M. Chemical gated field effect transistor by hybrid integration of one-dimensional silicon nanowire and two-dimensional tin oxide thin film for low power gas sensor. *ACS Appl. Mater. Interfaces* **2015**, *7*, 21263–21269.

[32] Zhang, Y.; Kolmakov, A.; Chretien, S.; Metiu, H.; Moskovits, M. Control of catalytic reactions at the surface of a metal oxide nanowire by manipulating electron density inside it. *Nano Lett.* **2004**, *4*, 403–407.

[33] Feng, P.; Shao, F.; Shi, Y.; Wan, Q. Gas sensors based on semiconducting nanowire field-effect transistors. *Sensors (Basel)* **2014**, *14*, 17406–17429.

[34] Zhou, X. Y.; Wang, Y.; Wang, J. X.; Xie, Z.; Wu, X. F.; Han, N.; Chen, Y. F. Amplifying the signal of metal oxide gas sensors for low concentration gas detection. *IEEE Sens. J.* **2017**, *17*, 2841–2847.

[35] Tonezzer, M. Selective gas sensor based on one single SnO_2 nanowire. *Sens. Actuat. B Chem.* **2019**, *288*, 53–59.

[36] Thai, N. X.; Van Duy, N.; Hung, C. M.; Nguyen, H.; Tonezzer, M.; Van Hieu, N.; Hoa, N. D. Prototype edge-grown nanowire sensor array for the real-time monitoring and classification of multiple gases. *J. Sci. Adv. Mater. Dev.* **2020**, *5*, 409–416.

[37] Afshar, M.; Preiß, E. M.; Sauerwald, T.; Rodner, M.; Feili, D.; Straub, M.; König, K.; Schütze, A.; Seidel, H. Indium-tin-oxide single-nanowire gas sensor fabricated via laser writing and subsequent etching. *Sens. Actuat. B Chem.* **2015**, *215*, 525–535.

[38] Chen, X. X.; Shen, Y. B.; Zhang, W.; Zhang, J.; Wei, D. Z.; Lu, R.; Zhu, L. J.; Li, H. S.; Shen, Y. S. In-situ growth of ZnO nanowire arrays on the sensing electrode via a facile hydrothermal route for high-performance NO_2 sensor. *Appl. Surf. Sci.* **2018**, *435*, 1096–1104.

[39] Ahn, J. H.; Yun, J.; Choi, Y. K.; Park, I. Palladium nanoparticle decorated silicon nanowire field-effect transistor with side-gates for hydrogen gas detection. *Appl. Phys. Lett.* **2014**, *104*, 013508.

[40] Kim, D.; Park, C.; Choi, W.; Shin, S. H.; Jin, B.; Baek, R. H.; Lee, J. S. Improved long-term responses of Au-decorated Si nanowire FET sensor for NH_3 detection. *IEEE Sens. J.* **2020**, *20*, 2270–2277.